actuators

MDPI

Article

Optimal Design Method of Post-Assembly Magnetizing Device with Field–Circuit Coupling Analysis

Zi-Ang Zhu [1], Yun-Chong Wang [1,2], Xue-Fei Qin [3], Lei Yao [1], Johan Gyselinck [4] and Jian-Xin Shen [1,2,*]

1 College of Electrical Engineering, Zhejiang University, Hangzhou 310027, China; ziang_zhu@zju.edu.cn (Z.-A.Z.); wangycee@zju.edu.cn (Y.-C.W.); lei_yao@zju.edu.cn (L.Y.)
2 Zhejiang Provincial Key Laboratory of Electrical Machine Systems, Hangzhou 310027, China
3 Zhejiang Windey Co., Ltd., Hangzhou 311106, China; xuefeiqin@zju.edu.cn
4 Bio Electro and Mechanical Systems Department, Université Libre de Bruxelles, 1000 Brussels, Belgium; johan.gyselinck@ulb.be
* Correspondence: J_X_Shen@zju.edu.cn; Tel.: +86-135-1672-0885

Abstract: Post-assembly magnetization can significantly simplify the manufacturing of the rotor of permanent magnet (PM) electrical machines. The optimization of the post-assembly magnetizing device using finite element analysis (FEA) is time-consuming; therefore, a globally optimal solution aiming at achieving an adequate magnetizing level and minimal energy consumption is difficult to achieve. In this paper, a field–circuit coupling analysis (FCCA) model is proposed to optimize the auxiliary stator-type magnetizing device for interior permanent magnet synchronous machines (IPMSMs). A reasonable simplification of the highly saturated magnetic circuit is made based on FEA results so that the magnetic equivalent circuit (MEC) model can be established. On the other hand, the eddy currents in the PMs are equivalent to an eddy current short-circuit; thus, by converting the field calculation into a circuit calculation, the time cost can be reduced significantly, which greatly improves the speed of multi-objective optimization of the magnetizing device with multiple degrees of freedom. A V-type IPMSM is taken as a study case, and its post-assembly magnetizing device is optimized with the proposed method. FEA and experimental results show that the PMs are fully magnetized, while the required energy consumption is greatly reduced when compared with an existing magnetizing device.

Keywords: magnetizing device; field–circuit coupling analysis; post-assembly magnetization; V-type IPMSM; optimal design

check for updates

Citation: Zhu, Z.-A.; Wang, Y.-C.; Qin, X.-F.; Yao, L.; Gyselinck, J.; Shen, J.-X. Optimal Design Method of Post-Assembly Magnetizing Device with Field–Circuit Coupling Analysis. *Actuators* **2023**, *12*, 383. https://doi.org/10.3390/act12100383

Academic Editors: Efren Diez-Jimeneze and Ignacio Valiente Blanco

Received: 1 September 2023
Revised: 29 September 2023
Accepted: 3 October 2023
Published: 11 October 2023

Copyright: © 2023 by the authors. Licensee MDPI, Basel, Switzerland. This article is an open access article distributed under the terms and conditions of the Creative Commons Attribution (CC BY) license (https://creativecommons.org/licenses/by/4.0/).

1. Introduction

Interior permanent magnet synchronous machines (IPMSMs) are widely utilized thanks to their outstanding advantages of high torque density and high efficiency. In the conventional manufacturing process, the permanent magnets (PMs) are magnetized before being assembled in the rotor. Strong magnetic forces then occur, making the process complicated, time-consuming, and risky of rotor component damage and personnel injury [1,2].

Post-assembly magnetization provides a solution to these problems. Unmagnetized magnets are inserted in the rotor, and then the latter are magnetized integrally with a dedicated magnetizing device. Due to the simple process and high safety with the unmagnetized magnets, post-assembly magnetization attracts growing attention.

Numerous post-assembly magnetization-related literature works have been published. Ferrite magnets can be easily magnetized with the machine stator winding, with the magnetization completeness depending on the PM shape [3]. The advantage of magnetization with the normal stator and its winding is that no additional equipment is required. For such a method, the magnetizing current is limited by the machine stator structure and, in particular, the mechanical strength of the winding. Thus, when rare-earth PMs are

adopted, a much higher field strength is required and the stator needs to be especially designed to withstand a sufficient current for magnetization. Different stator winding currents for magnetization are studied, and a magnetization field of 2.5 times the coercivity is found to be sufficient for the full magnetization of rare-earth PMs [4]; then, a rare-earth surface-mounted PM synchronous machine (SPMSM), which is post-assembly magnetized with its stator, is designed. In [5], to simplify the design process, the stator winding is simplified to a filamentary conductor with the same number of turns, which represents the center of the magnetomotive force (MMF), and the relative permeability of the highly saturated iron core is approximated to that of the air; then, the parameters of the machine winding are optimized to obtain a sufficient magnetizing field, while the influence of the core structure is disregarded. However, the stator winding needs to be stronger when the large magnetizing current is considered, which is in conflict with the machine volume, cost, and operation performance. Thus, several improved methods are proposed to satisfy the magnetization requirement of IPMSMs and large-power SPMSMs, whilst those methods should be chosen according to the machine structure and magnetic field strength required for the magnetization of the magnets. For example, integrated magnetizing coils are directly wound around the PM poles for the magnetization of large-power SPMSMs [6]. For line-start IPMSMs, the utilization and influence of the squirrel cage and the copper bars are investigated [7,8].

However, a more common approach for the post-assembly magnetization of rare-earth IPMSMs is to use a dedicated device composed of a magnetizer and a magnetizing fixture, which is also called an auxiliary stator. The eddy currents generated during the magnetizing process have attracted the attention of researchers. A three-dimensional finite element (FE) model is established to analyze the eddy currents inside the PMs and metal sleeves [9]; the results show that the eddy currents may reduce the magnetizing field, resulting in the failure of the PMs' magnetization. The impact of a soft magnetic material type of fixture is also compared [10]; the fixture using solid steel as the soft magnetic material consumes much more energy to generate a sufficient magnetizing field due to the induced eddy currents. Thus, the pulse-width is increased by optimizing the coil structure, in order to weaken the eddy currents [11,12]. For a line-start IPMSM, rotor bar dimensions are further researched, considering the induced currents in the squirrel cage [13]. The design process is further refined, where a preliminary design is made by deriving the required magnetic field energy when the magnets are fully magnetized, and then the coil turns and the capacitance of the magnetizer are focused on for optimization [14]. A similar two-step approach is also taken for the magnetization of V-type IPMSMs [15]; the winding structure is optimized with FE parametric modeling starting from a rough design, considering the influence of magnetizer capacitance and eddy currents in the PMs. A design method that has a fixed auxiliary stator structure during the optimization process is further compared with a design method with a fixed wire gauge [16]. The optimized structures of the magnetizing fixture obtained with the two methods are completely different, which illustrates that the parameters are mutually restrictive.

For these design processes, since the FEA is time-consuming, a few parameters are selected as degrees of freedom, and a local optimal solution is obtained to generate enough magnetizing field. However, the calculation method of the global optimal solution has not been proposed in the aforecited paper, as the minimization of energy consumption of the magnetizing device has not been considered. Therefore, an optimization method without FE parametric calculations is worth investigating.

In this paper, an auxiliary stator-type post-assembly magnetization device for a 1.3 kW, 15,000 r/min 6-slot 4-pole V-type IPMSM is investigated as a study case. Multi-parameter optimization is required to meet the design specifications and reduce the energy consumption, and a design approach based on the field–circuit coupling analysis (FCCA) is proposed. The magnetic equivalent circuit (MEC) models are improved to consider the highly saturated iron cores, and the eddy currents in the PMs are considered via an equivalent circuit model. The proposed design approach is used to optimize a magnetizing device, and the

FE method is used to confirm its performance. A prototype of the optimal design is made and compared with an existing magnetizing device that is being used in a factory.

2. Investigated Magnetizing Fixture and Design Guidelines

2.1. Structure of Investigated Post-Assembly Magnetizing Device

The post-assembly magnetizing device is composed of a magnetizing fixture and a magnetizer. For a fractional-slot machine such as the one investigated, its stator winding is unable to generate a magnetizing field corresponding to the rotor poles, which results in a lot of spatial harmonics and makes the magnetization process much more complicated [17]. Thus, a magnetizing fixture with the same number of poles as the investigated rotor is adopted as an auxiliary stator, which offers a convenient solution. For the ease of understanding, the auxiliary stator will be referred to as the magnetizing fixture for the remainder of this article. Unmagnetized PMs are assembled in the rotor core of the IPMSM and then magnetized as a whole. The parameters of the investigated rotor are shown in Table 1. A quarter cross-section of the auxiliary stator and the rotor is shown in Figure 1a. The coils of the auxiliary stator are connected to the magnetizer, whose power circuit structure is shown in Figure 1b and the current pulse is generated. When thyristor SCR1 is turned on, the capacitor is charged to a high voltage through the transformer and the diode rectifier, with SCR1 turning off automatically at the end of the charging. Then, when thyristor SCR2 is turned on, the capacitor is discharged, serving as a pulse power supply. The power diode in reverse parallel is used to ensure that the capacitor energy is completely drained without oscillation.

Table 1. Parameters and ratings of the investigated IPMSM.

Parameter Name	Parameter Value
Power	1300 W
Speed	15,000 r/min
Number of poles	4
Rotor outer diameter	42 mm
Rotor stack length	46.2 mm
Magnet thickness	2.8 mm
Magnet width	11.2 mm
Iron core material	FeSi laminations
PM material	Nd-Fe-B (N42SH)

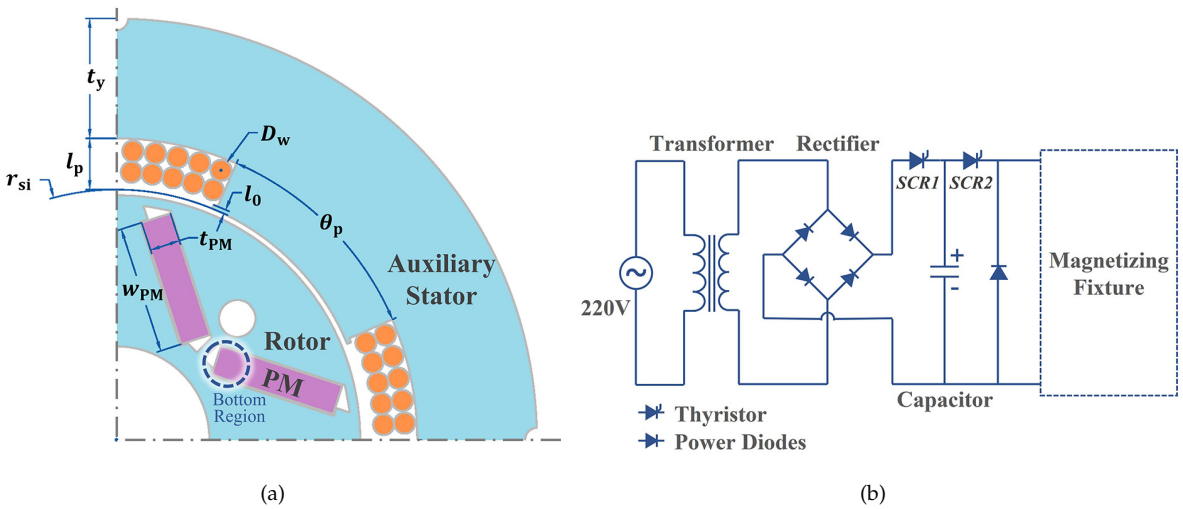

(a) (b)

Figure 1. Auxiliary stator-type post-assembly magnetizing device: (**a**) Quarter cross-section of the rotor to be magnetized and the auxiliary stator. (**b**) Power circuit structure of magnetizer.

2.2. Design Guidelines

For Nd-Fe-B magnets, it is recognized that a peak flux density value (reached at some instant during the magnetization) of 3 T is sufficient [2,14]. In this paper, the region at the bottom of the V-type PMs is focused on due to the difficulty to magnetize. In this paper, the doubled time that the charging current takes to rise from zero to the peak is further referred to as the magnetization pulse width T_M, which should be sufficiently long for the domain rotation of the PMs.

The permeability of the iron core is approximated as the one of air during the magnetization pulse in some papers. However, for higher accuracy, the B–H curve of the FeSi laminations needs to be considered. Due to the rapid change of the magnetizing field, eddy currents are induced in the PMs, weakening the magnetizing field. The eddy currents in the iron cores are neglected here because they are much smaller than those of magnet blocks. The electrical conductivity of the Nd-Fe-B material is assumed to be 0.625 MS/m.

The airgap between the auxiliary stator and the investigated rotor should be as small as possible to strengthen the magnetizing field, and 0.5 mm is selected as the airgap length. For the magnetizing winding, it is imperative to use thickly insulated copper wires to withstand the high currents. Additionally, employing epoxy resin curing for stabilizing the winding is crucial to prevent deformation resulting from the stress of the current, particularly at the winding end coils. These requirements limit the potential use of the machine stator winding for magnetizing PMs, considering both the manufacturing cost and their impact on the machine performance.

The number of turns per coil N is restricted by the wire gauge and the slot dimensions. To make full use of the slot space, the number of coil layers N_{layer} is:

$$N_{layer} = \left\lfloor K_s \frac{8(l_p - l_0)}{D_w} \right\rfloor \tag{1}$$

where the operator $\lfloor\rfloor$ represents rounding down, K_s is the coefficient to adjust the slot fill factor considering main insulation, l_p is the pole length, l_0 is the length of the pole shoe, and D_w is the wire diameter considering inter-turn insulation; see Figure 1a. Due to the non-parallel slot walls, the number of turns in each layer is generally different; thus, the total number of turns is given by:

$$N = \sum_{n=1}^{N_{layer}} \left\lfloor K_s \pi \left(\frac{1}{2p} - \frac{\theta_p}{360^\circ} \right) \frac{r_{si} + l_0 + (n-1)D_w}{D_w} \right\rfloor \tag{2}$$

with p the number of pole pairs, θ_p the pole width angle, and r_{si} the inner radius of the auxiliary stator.

The device is supposed to fully magnetize the PMs while minimizing the energy consumption W_M. As the magnetizer is completely discharged after the magnetization, the energy consumption is equal to the energy initially stored in the capacitor:

$$W_M = \frac{1}{2} C {U_C}^2 \tag{3}$$

with C the magnetizer capacitance, and U_C the discharging voltage.

It has been verified via simulation that a specific peak value of flux density can be achieved with either a smaller capacitance but higher voltage or a larger capacitance but lower voltage. However, the former would lead to a lower pulse width T_M and a lower copper loss during the rising of the current. Therefore, these magnetizers have advantages in W_M compared with the latter. However, T_M has a minimum value, as mentioned above. It is necessary to ensure a sufficiently high T_M while minimizing W_M.

Six parameters remain as degrees of freedom for the optimization: θ_p, l_p, yoke thickness t_y, D_w, C, and U_C. The first four parameters define the structure of the auxiliary stator along with the inductance and resistance of its winding. Pulse width T_M and the complete-

ness of magnetization depend on all six parameters, and the best parameter combination is searched based on the FCCA method.

3. Equivalent Models and Field–Circuit Coupling Analysis

3.1. Magnetic Equivalent Circuit Model of Rotor

The IPMSM rotor with V-type magnets has a complex geometry. The distances from each part of the magnets to the outer surface of the rotor are different. Thus, it is difficult to establish the MEC model directly, and FEA is used to aid in the modeling.

The outer surface of the one-eighth rotor is divided into six segments as shown in Figure 2. The dashed line indicates the dividing line of the flux, which enters the rotor at each segment when the core is saturated. The flux through each segment is denoted by φ_{r1} to φ_{r6}. Taking the right radial boundary of the model as the zero-potential surface, the average magnetic potential drop is denoted by F_{r1} to F_{r6}. According to the rotor geometry, the rotor is simplified to several reluctances connected in parallel, which are denoted by R_{rotori}, R_{PM}, and R_{Barrier} in Figure 3. As the permeability of the PMs is much smaller than the one of the unsaturated silicon steel, the reluctances of the PMs and the magnetic barriers are especially denoted to clarify the magnetic circuit under different saturation conditions. Each of the reluctances is defined by the cross-section area S_R and length l_R:

$$F_R = f(\varphi_R / S_R) \cdot l_R \tag{4}$$

with F_R the potential drop on the reluctance, φ_R the flux through the reluctance, and f the $H(B)$ function of the different materials. Then, the potential drop of each segment is calculated as:

$$\begin{cases} F_{r1} = F_{R_{\text{rotor1}}} + F_{R_{\text{PM}}} \\ \quad \cdots \\ F_{r5} = F_{R_{\text{rotor5}}} + F_{R_{\text{PM}}} \\ F_{r6} = F_{R_{\text{rotor6}}} \\ F_{R_{\text{PM}}} = F_{R_{\text{Barrier}}} \end{cases} \tag{5}$$

The shape of the PMs and the magnetic barriers is regular so that their dimensions are readily substituted into the reluctance formula as S_R and l_R, while the irregular shape of the iron core complicates the parameter determination. FEA is used to calculate F_{rj} and φ_{rj} of each segment under different currents. F_{rj} is obtained by integrating H from the zero-potential surface to the rotor surface, and φ_{rj} is obtained by integrating B on the segment of the rotor surface. Then, the FEA results are obtained and parametric regression is adopted to calculate the undetermined parameters. In this way, the MEC model is established.

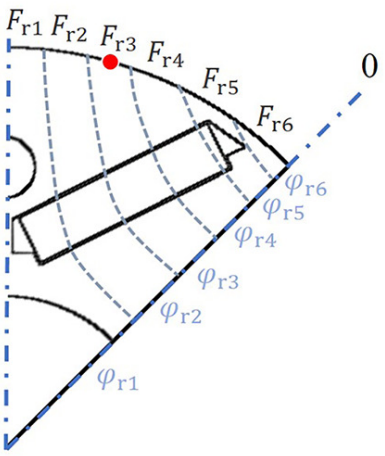

Figure 2. One-eighth model of rotor flux distribution with saturated iron core.

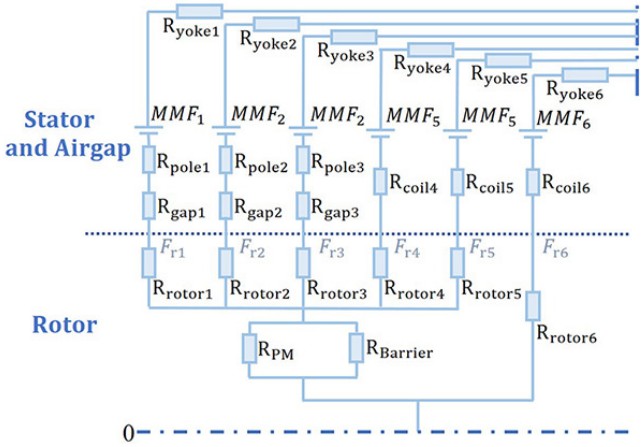

Figure 3. MEC model of rotor and auxiliary stator.

The influence of the auxiliary stator structure on the rotor MEC model is also considered. The middle point of the third surface segment is selected as the test point, see the red dot in Figure 2. Flux φ_{r3} is replaced by the normal magnetic flux density B_{r3}, and the B_{r3}–F_{r3} curves with different pole lengths and pole widths are compared in Figure 4. Obviously, the pole width has a significant influence on the curve, whereas the effect of pole length can be neglected. Thus, it is needed to calculate S_R and l_R under different pole widths. Then, the curves of these two parameters as a function of pole width are obtained via interpolation.

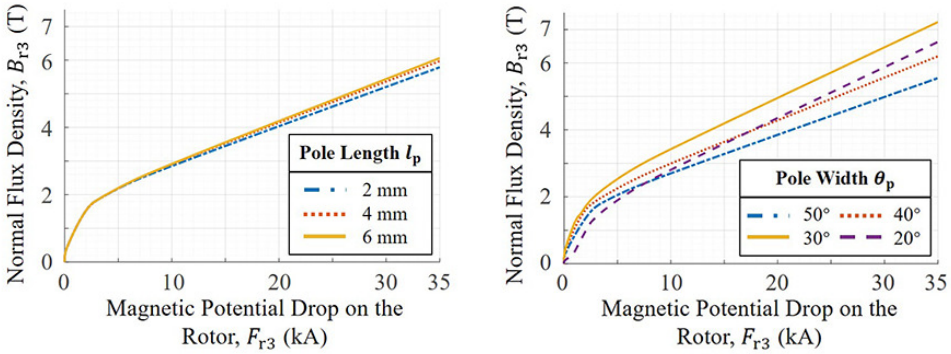

Figure 4. Influence of auxiliary stator structure on the rotor MEC model: (**a**) B_{r3}–F_{r3} curve with different pole widths and 4.4 mm pole length. (**b**) B_{r3}–F_{r3} curve with different pole lengths and 23.5° pole width.

3.2. Magnetic Equivalent Circuit Model of Stator

The structure of the auxiliary stator is relatively simple and is defined with several degrees of freedom. In Figure 5, the magnetic circuit of the auxiliary stator is saturated and divided into six branches, with the latter categorized into two types. The first type of branches closes through the airgap, stator pole, and yoke, while the second type closes through the airgap, slot, and yoke. The permeability of the coils in the slot is assumed the same as air so that the two parts are merged. Each branch is simplified to several reluctances and a source of MMF connected in series as shown in Figure 3. The formula of reluctance is the same as the rotor MEC model, and the source of magnetomotive force $MMF = K_N NI$, with K_N the proportion of the half coil enclosed by the branch, N the number of turns per half coil, and I the value of the current. For the first type of magnetic circuit, K_N is equal to 1.

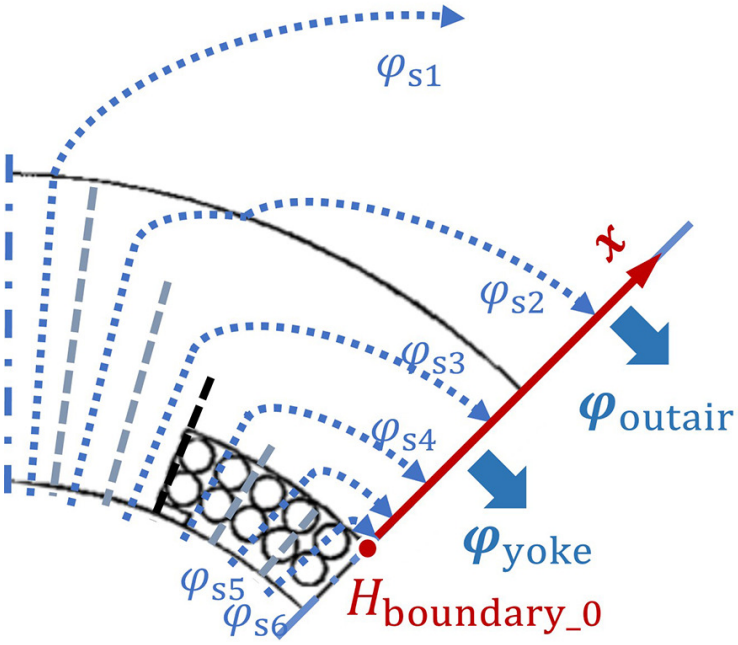

Figure 5. One-eighth model of auxiliary stator flux distribution when iron core is being saturated.

In the traditional MEC method and with a normal level of core saturation, the second type of branches is neglected. For the study at hand, with the peak flux density in the stator core exceeding 5 T during the magnetization, it is necessary to consider the flux branches through the air. When the core is highly saturated, the flux density distribution is significantly different from the unsaturated condition, especially in the stator yoke and slot. Thus, several coefficients are proposed to make the MEC model suitable for both situations.

In the stator yoke and the air outside the stator, the flux circumferentially passes the symmetrical boundary. To simplify the model, the magnetic field strength on the boundary H_{boundary} is assumed to decay as an inversely proportional function with the radius of the flux lines:

$$H_{\text{boundary}}(x) = \frac{r_{\text{si}} + l_{\text{p}}}{r_{\text{si}} + l_{\text{p}} + x} H_{\text{boundary}_0} \tag{6}$$

with x the distance from the inner radius of the yoke, and H_{boundary_0} the magnetic field strength on the inner radius of the yoke. Then, the flux φ_{yoke} passing the boundary through the yoke reads:

$$\varphi_{\text{yoke}} = l_{\text{rotor}} \int_0^{t_{\text{y}}} f_{\text{sl}}\Big(H_{\text{boundary}}(x)\Big)\mathrm{d}x \tag{7}$$

with f_{sl} the $H(B)$ relation of the laminations, and l_{rotor} the rotor stack length. The air outside the stator deserves attention as an external circuit when the core is saturated. A thick enough section of air circuit is used to calculate the flux passing through the air φ_{outair}:

$$\varphi_{\text{outair}} = l_{\text{rotor}} \int_{t_{\text{y}}}^{t_{\text{y}}+t_{\text{air}}} \mu_0 H_{\text{boundary}}(x)\mathrm{d}x \tag{8}$$

where μ_0 is the permeability of vacuum, and t_{air} the adopted empirical value of the air thickness, with the latter determined as one-eighth of the outer circumference of the stator:

$$t_{\text{air}} = \pi\left(r_{\text{si}} + l_{\text{p}} + t_{\text{y}}\right)/2p \tag{9}$$

The air outside the stator is equivalent to an additional yoke. The total equivalent thickness $t_{\text{y}_{\text{eq}}}$ satisfies:

$$l_{\text{rotor}} \int_0^{t_{\text{y}_{\text{eq}}}} f_{\text{sl}}\Big(H_{\text{boundary}}(x)\Big)\mathrm{d}x = \varphi_{\text{yoke}} + \varphi_{\text{air}} \tag{10}$$

The sum of the flux flowing through each branch is equal to the flux passing through the boundary:

$$\sum_{j=1}^{6} \varphi_{sj} = \varphi_{\text{yoke}} + \varphi_{\text{air}} \tag{11}$$

with φ_{sj} the flux of the jth stator magnetic branch. Then, the yoke width occupied by each branch is calculated based on the distribution of H_{boundary}, and the yoke reluctances lof the branches are obtained.

In the stator slots, the flux passes in parallel to the pole and then becomes curved with increasing saturation level. Figure 6a illustrates a magnetic branch when the core is saturated. The gray line is the cross-section of the branch at the interface of the yoke and slot, and the black dot is the center of the branch region in the slot. There is a deviation from the dot to the perpendicular bisector of the cross-section, which means that the proportion of the coil enclosed by the flux is affected by the bending of flux lines. The deviation is measured to guarantee the accuracy of MMF and flux linkage. The curved flux line is assumed to be a circle arc, as shown in Figure 6b. The tangential flux density of the jth branch at the midpoint of the cross-section $B_{\text{tan}j}$ is:

$$B_{\text{tan}j} = \frac{\sum_{k=1}^{j} \varphi_{sk} - \varphi_{sj}}{\sum_{k=1}^{6} \varphi_{sk}} B_{\text{yoke}_0} \tag{12}$$

with B_{yoke_0} the flux density on the inner radius of the yoke,

$$B_{\text{yoke}_0} = f_{\text{sl}}\left(H_{\text{boundary}_0}\right) \tag{13}$$

and the normal flux density of the j^{th} branch at the midpoint of the cross-section $B_{\text{nor}j}$ is:

$$B_{\text{nor}j} = \varphi_{sj} / S_{\text{nor}j} \tag{14}$$

with $S_{\text{nor}j}$ the the cross-section area. According to the trigonometric relationship, the angular offset of the j^{th} branch $\theta_{\text{offset}j}$ is:

$$\theta_{\text{offset}j} = \frac{\sqrt{B_{\text{nor}j}^2 + B_{\text{tan}j}^2} - B_{\text{nor}j}}{B_{\text{tan}j}} \frac{l_{\text{p}}/2}{r_{\text{si}} + l_{\text{p}}/2} \tag{15}$$

Therefore, the proportion of the coil enclosed by the j^{th} branch is:

$$K_{\text{N}j} = \begin{cases} 1 & , \theta_{\text{offset}j} + \theta_j > \theta_{\text{s}} \\ \left(\theta_{\text{offset}j} + \theta_j\right)/\theta_{\text{s}} & , \theta_{\text{offset}j} + \theta_j < \theta_{\text{s}} \end{cases} \tag{16}$$

where θ_j is the angle corresponding to the perpendicular bisector of the j^{th} cross-section, and θ_{s} is the angle corresponding to the slot width, which is:

$$\theta_{\text{s}} = \left(90 - \theta_{\text{p}}\right)/2 \tag{17}$$

With the proposed improvements, the calculations of the MMF and the reluctances are suitable for different saturation conditions. Further, the results under different numbers of equivalent circuit branches are compared. We observe little difference when more than three branches are considered. Thus, it is recommended to contain three branches in the MEC model to reduce the calculation time. At least one branch of each type is required, and the type of the remaining one is determined according to the pole width.

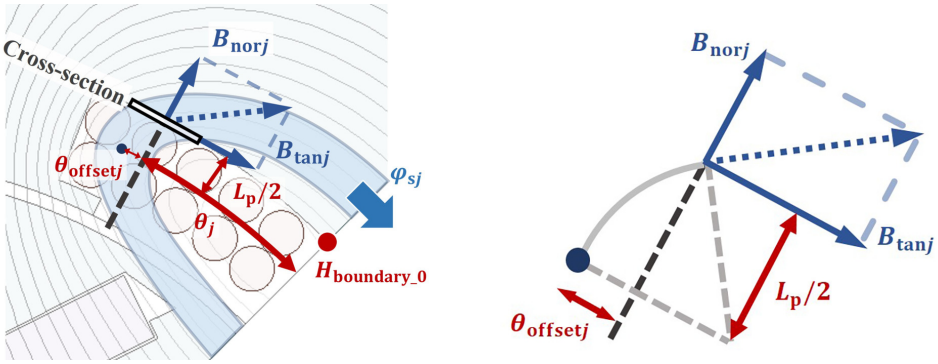

(a) (b)

Figure 6. Distribution of flux lines around the auxiliary stator slot: (**a**) One of the magnetic branches with saturated iron core. (**b**) Geometric relationship of $\theta_{\text{offset}j}$, $B_{\text{tan}j}$, and $B_{\text{nor}j}$.

3.3. Equivalent Circuit of Eddy Currents in Permanent Magnet

In this section, the analytical method is taken to evaluate the reaction of PM eddy currents to the applied magnetizing field. Then, an RL series circuit is used as the equivalent eddy current circuit to approximate the analytical results. Based on Maxwell's equations, the basic field equation in a PM is:

$$\nabla^2 \boldsymbol{H}_{\mathbf{PM}} = \mu_{\text{PM}} \gamma_{\text{PM}} \frac{\partial \boldsymbol{H}_{\mathbf{PM}}}{\partial t} \tag{18}$$

where $\boldsymbol{H}_{\mathbf{PM}}$ is the magnetic field strength in PMs; μ_{PM} and γ_{PM} are the permeability and electrical conductivity of PMs. To simplify the analysis, several assumptions are made:

1. The applied magnetic field is uniform and perpendicular to the surface of the PMs.
2. μ_{PM} and γ_{PM} are constant.

Thus, a two-dimensional (2D) field on the x–y plane of local coordinate is used as the solution domain, as shown in Figure 7. The $\boldsymbol{H}_{\mathbf{PM}}$ has the component in the z-direction only, denoted by H_{PM}, which satisfies:

$$\frac{\partial^2 H_{\text{PM}}(x,y,t)}{\partial x^2} + \frac{\partial^2 H_{\text{PM}}(x,y,t)}{\partial y^2} = \mu_{\text{PM}} \gamma_{\text{PM}} \frac{\partial H_{\text{PM}}(x,y,t)}{\partial t} \tag{19}$$

The boundary and initial conditions are:

$$\begin{cases} H_{\text{PM}}(\pm l_{\text{PM}}/2, y, t) = H_0(t) \\ H_{\text{PM}}(x, \pm w_{\text{PM}}/2, t) = H_0(t) \\ H_{\text{PM}}(x, y, 0) = 0 \end{cases} \tag{20}$$

with l_{PM} the length of PMs, w_{PM} the width of PMs, and H_0 the magnetic field strength of the applied magnetizing field. The method of separation of variables [18] is used to solve the equations. H_{PM} is expanded into a Fourier series, and the unit impulse response function h_{PM} is derived as:

$$h_{\text{PM}}(x,y,t) = \sum_{\substack{m=1,3,5,\cdots \\ n=1,3,5,\cdots}}^{\infty} \frac{K_{mn}}{\tau_{mn}} \cos\frac{m\pi x}{l_{\text{PM}}} \cos\frac{n\pi y}{w_{\text{PM}}} e^{-t/\tau_{mn}} \tag{21}$$

with K_{mn} the magnitude of the Fourier coefficient, τ_{mn} the decay time constant:

$$K_{mn} = \frac{16}{mn\pi^2} \sin\frac{m\pi}{2} \sin\frac{n\pi}{2} \tag{22}$$

$$\tau_{mn} = \frac{\mu_{\mathrm{PM}}\gamma_{\mathrm{PM}}}{\pi^2\left(\frac{m^2}{l_{\mathrm{PM}}} + \frac{n^2}{w_{\mathrm{PM}}}\right)} \tag{23}$$

The Fourier series in (21) is composed of sinusoidal plane waves of order m in the x direction and order n in the y direction. With the increase in the spatial order, the sinusoidal waves have smaller decay time constants.

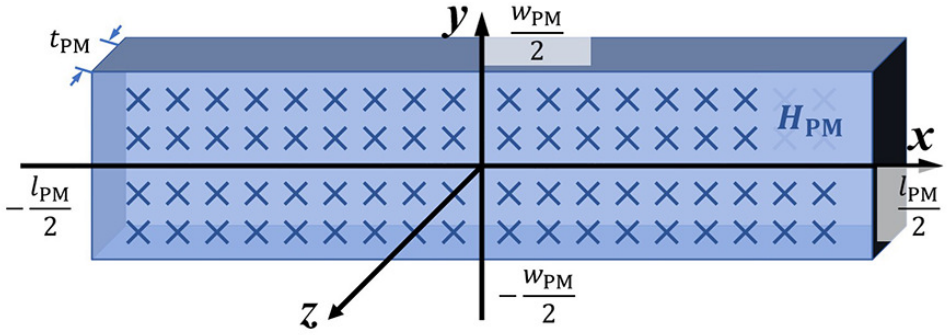

Figure 7. The 2D magnetic field within the x–y plane of PMs.

A half-sinusoidal magnetic field with the pulse width of T and the amplitude of H_{mag} is assumed to be applied to the PMs. By the Duhamel's integral,

$$H_{\mathrm{PM}}(x,y,t) = \int_0^t H_{\mathrm{mag}} \sin\frac{\pi\tau}{T} h_{\mathrm{PM}}(t-\tau)\mathrm{d}\tau \tag{24}$$

Therefore,

$$H_{\mathrm{PM}}(x,y,t) = H_{\mathrm{mag}} \sin\frac{\pi t}{T} - H_{\mathrm{mag}} \sum_{\substack{m=1,3,5,\cdots \\ n=1,3,5,\cdots}}^{\infty} K_{mn} C_{mn}(t) \cos\frac{m\pi x}{l_{\mathrm{PM}}} \cos\frac{n\pi y}{w_{\mathrm{PM}}} \tag{25}$$

with C_{mn} the time coefficient, which varies with the orders:

$$C_{mn}(t) = \frac{\pi}{T}\tau_{mn} \cdot \frac{\frac{\pi}{T}\tau_{mn}\sin\frac{\pi t}{T} + \cos\frac{\pi t}{T} - e^{-t/\tau_{mn}}}{1 + \left(\frac{\pi}{T}\tau_{mn}\right)^2} \tag{26}$$

The first term of H_{PM} in (25) is the applied field, and the second term is the reaction field of eddy currents in the Fourier series. The first two terms of C_{mn} are the steady state components, which are sine waves that lag behind the applied field. And the third term is the transient component, which decays exponentially.

Further, the flux counteracted by the reaction field of PMs φ_{re} is:

$$\varphi_{\mathrm{re}} = \varphi_{\mathrm{mag_{PM}}} \sin\frac{\pi t}{T} - \mu_{\mathrm{PM}} \iint H_{\mathrm{PM}}(x,y,t)\,\mathrm{d}x\,\mathrm{d}y \tag{27}$$

where:

$$\varphi_{\mathrm{mag_{PM}}} = \mu_{\mathrm{PM}} l_{\mathrm{PM}} w_{\mathrm{PM}} H_{\mathrm{mag}} \tag{28}$$

Therefore,

$$\varphi_{\mathrm{re}} = \frac{16}{\pi^2}\varphi_{\mathrm{mag_{PM}}} \sum_{\substack{m=1,3,5,\cdots \\ n=1,3,5,\cdots}}^{\infty} \frac{C_{mn}(t)}{m^2 n^2} \tag{29}$$

The total counteracted flux can be decomposed into the spatial harmonics of different orders, whose amplitude decrease rapidly with the increasing orders.

Equivalent eddy current circuit is used to simulate the reaction field of the PMs. A unit circuit consisting of a resistance R_u and an inductance L_u will generate an equivalent eddy current i_u as well as the counteracted flux $\widehat{\varphi}_{ru}$ when an induced electromotive force E_u is applied:

$$L_u \frac{di_u}{dt} + R_u i_u = E_u \tag{30}$$

$$\widehat{\varphi}_{ru} = L_u i_u \tag{31}$$

Therefore,

$$\widehat{\varphi}_{ru} = \varphi_{mag_{PM}} \frac{\pi}{T} \frac{L_u}{R_u} \frac{\frac{\pi}{T}\frac{L_u}{R_u} \sin \omega t + \cos \omega t - e^{-\frac{R_u}{L_u} t}}{1 + \left(\frac{\pi}{T}\frac{L_u}{R_u}\right)^2} \tag{32}$$

Comparing the counteracted flux obtained by the analytical method and unit-equivalent eddy current circuit, $\widehat{\varphi}_{ru}$ has a similar formula structure with C_{mn}. Thus, any spatial harmonic of the counteracted flux can be represented by a unit equivalent circuit with a resistance R_{umn} and an inductance L_{umn}, which satisfies:

$$\frac{L_{umn}}{R_{umn}} = \tau_{mn} \tag{33}$$

Despite the unit-equivalent circuit accurately representing the counteracted flux of each spatial order, an equivalent circuit composed of $m \times n$ unit circuits is complicated and the computation will be time-consuming. An aggregate equivalent circuit with the same structure of the unit circuit is proposed as an alternative:

$$L_e \frac{di_e}{dt} + R_e i_e = E_e \tag{34}$$

with L_e the inductance of the aggregate equivalent circuit, i_e the equivalent eddy current, R_e the resistance which varies with the frequency of applied magnetic field, and E_e the induced electromotive force. In the aggregate equivalent circuit, the eddy currents are equivalent to flowing along the edge of the PMs; thus, the E_e and L_e are:

$$E_e = \frac{d}{dt}\left(\varphi_{mag_{PM}} \sin \frac{\pi t}{T}\right) \tag{35}$$

$$L_e = \mu_{PM} l_{PM} w_{PM} / t_{PM} \tag{36}$$

with t_{PM} the thickness of the PM.

Due to the multiple spatial harmonics contained in the total counteracted flux, (33) is not suitable for the aggregate equivalent eddy current circuit. Thus, R_e is calculated with parametric regression to make the results obtained with the equivalent circuit close to the analytical results.

In Figure 8, φ_{re} under different frequencies is analyzed with (29), and the $\widehat{\varphi}_{re}$ calculated with the equivalent eddy current circuit and the corresponding R_e is compared. When the frequency of the applied field is close to 100 kHz, the spatial harmonics of low orders, such as the 3rd and 5th, cannot be ignored and have waveforms different from the fundamental one. Thus, there is a deviation between the analytical method and equivalent circuit. The accuracy of the aggregate equivalent circuit can be improved by increasing the number of unit equivalent circuits at such a frequency. However, as the magnetization process requires an adequate pulse width of the order of a millisecond, the magnetizing field time-harmonics at the frequencies close to 100 kHz are insignificant and the aggregate equivalent circuit has a sufficient accuracy for such a scenario. The curve of R_e with the

frequency of the applied field is plotted in Figure 8e. The variation of R_e below 100 kHz is relatively little, which means that R_e can be regarded as a constant.

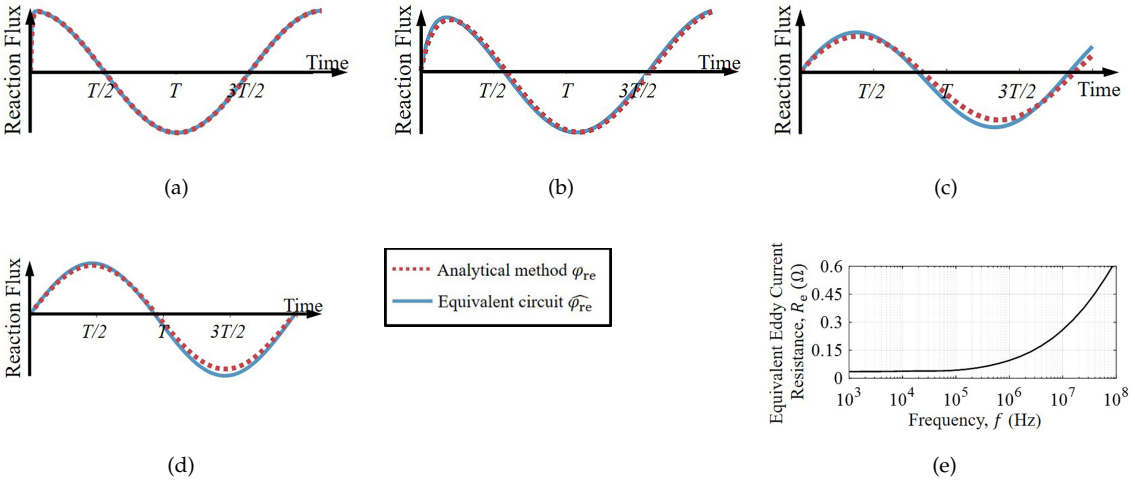

Figure 8. Comparison between φ_{re} and $\widehat{\varphi}_{re}$ at different frequencies: (**a**) Reaction flux with $f = 1$ kHz and $R_e = 35.8\,m\Omega$. (**b**) Reaction flux with $f = 10$ kHz and $R_e = 37.2\,m\Omega$. (**c**) Reaction flux with $f = 100$ kHz and $R_e = 42.5\,m\Omega$. (**d**) Reaction flux with $f = 1$ MHz and $R_e = 90.0\,m\Omega$. (**e**) Variation of R_e with frequency.

3.4. Field–Circuit Coupling Analysis

The magnetization process is actually the discharge of a magnetizing circuit as shown in Figure 9, where $i(t)$ is the instantaneous magnetizing current, $u_C(t)$ is the instantaneous capacitor voltage, with initial value U_C, and R_{coil} is the resistance of the coil. The latter is related to the number of turns N and the wire gauge as follows:

$$R_{coil} = 4pNl_m / (\gamma_{copper} S_{wire}) \tag{37}$$

with γ_{copper} the electrical conductivity of copper, l_m the stack length of the magnetizer, and S_{wire} the cross-section area of the wire.

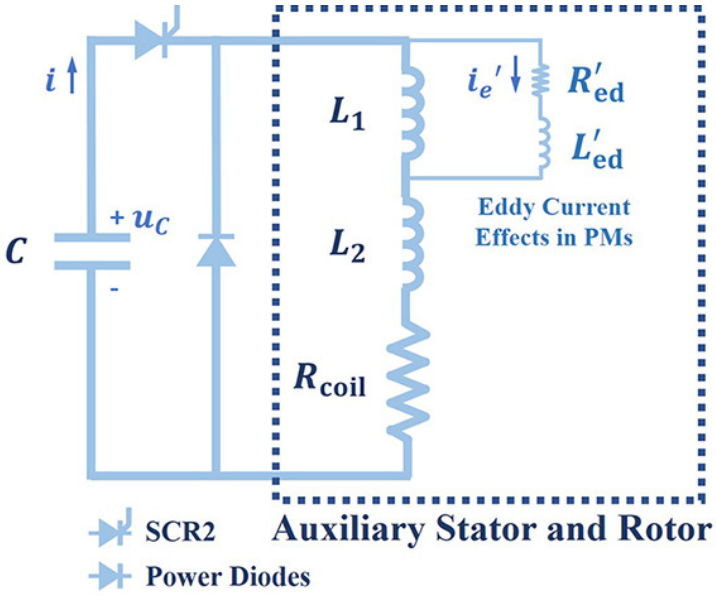

Figure 9. Equivalent electric circuit model considering the eddy currents.

The MEC models of the rotor and auxiliary stator are connected to calculate the flux linkage. The stator circuit segmentation is decided by pole width, and then rotor segmentation is adjusted accordingly. The parameters of the adjusted rotor MEC model are obtained via parameter smoothing based on the rotor MEC model studied in Section 2.

Then, the flux φ_{sj} in each branch considering different magnetizing currents I is calculated with the Newton–Raphson method. The flux linkage Ψ is:

$$\Psi(I) = 2p\sum_{i} K_{Nj} N \varphi_{sj}(I) \tag{38}$$

from which, the resulting current-dependent inductance $L(I) = \Psi(I)/I$ is obtained. The eddy currents are generated by the varying flux through the PMs $\varphi_{R_{PM}}$; this is similar to the induced current in the short-circuited secondary winding of a transformer. The inductance corresponding to $\varphi_{R_{PM}}$ is denoted by L_1:

$$L_1(I) = \frac{4pK_{N_{PM}} N \varphi_{R_{PM}}(I)}{I} \tag{39}$$

with $K_{N_{PM}}$ the average proportion of coils surrounded by the magnetic circuits through the PMs. Then, the inductance corresponds to the remainder of the part $L_2(I) = L(I) - L_1(I)$.

R'_e, L'_e, and i'_e are the reduction values of the equivalent eddy resistance, inductance, and current on the coil side, which are converted from the equivalent eddy current circuit:

$$R'_e = 4p\left(K_{N_{PM}} N\right)^2 R_e \tag{40}$$

$$L'_e = 4p\left(K_{N_{PM}} N\right)^2 L_e \tag{41}$$

Based on the magnetizing circuit, the equations of the magnetization process after turning on the thyristor SCR2 are divided into two stages. When the capacitor is discharging:

$$\begin{cases} \dfrac{\mathrm{d}[L_1(i - i'_e) \cdot (i - i'_e)]}{\mathrm{d}t} + \dfrac{\mathrm{d}[L_2(i) \cdot i]}{\mathrm{d}t} = u_C - R_{coil} i \\ \dfrac{\mathrm{d}[L_1(i - i'_e) \cdot (i - i'_e)]}{\mathrm{d}t} - \dfrac{\mathrm{d}[L'_e(i'_e) \cdot i'_e]}{\mathrm{d}t} = R'_e i'_e \\ C\dfrac{\mathrm{d}u_C}{\mathrm{d}t} = i \end{cases} \tag{42}$$

After the capacitor is completely discharged, the power diode in reverse parallel turns on and thyristor SCR2 turns off:

$$\begin{cases} \dfrac{\mathrm{d}[L_1(i - i'_e) \cdot (i - i'_e)]}{\mathrm{d}t} + \dfrac{\mathrm{d}[L_2(i) \cdot i]}{\mathrm{d}t} = -R_{coil} i \\ \dfrac{\mathrm{d}[L_1(i - i'_e) \cdot (i - i'_e)]}{\mathrm{d}t} - \dfrac{\mathrm{d}[L'_e(i'_e) \cdot i'_e]}{\mathrm{d}t} = R'_e i'_e \\ u_C = 0 \end{cases} \tag{43}$$

Since the inductance varies with the current, the equations are discretized and solved iteratively. The results obtained are verified with the FE method. Figure 10 shows the operating parameters calculated with FEA and FCCA. The accuracy and efficiency of the FCCA method are demonstrated by how closely the FCCA results match those of the FEA.

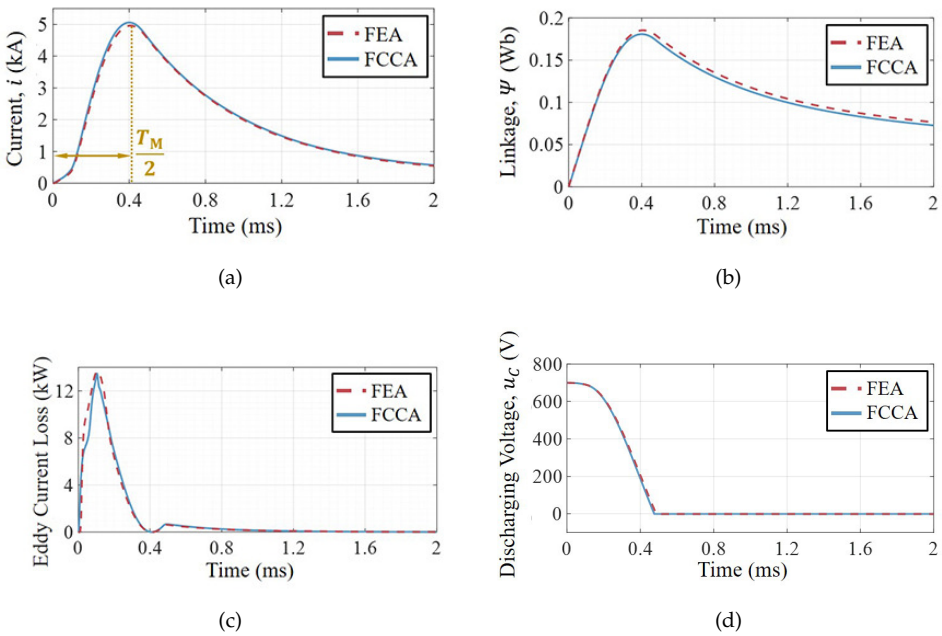

Figure 10. Dynamic results obtained with FCCA and FEA: (**a**) Current with time. (**b**) Flux linkage with time. (**c**) Eddy currents losses with time. (**d**) Capacitor voltage with time.

4. Optimization Design of Auxiliary Stator-Type Magnetizing Device

The stages of the design method proposed in this paper are illustrated in Figure 11. The PM equivalent eddy current circuit and rotor MEC model are simplified from the rotor to be magnetized. The stator MEC model is established according to the auxiliary stator structure, which is decided by multiple degrees of freedom. And the transient analysis is carried out according to the FCCA model with the software MATLAB R2021a. The FCCA greatly reduces the time consumption for magnetizing simulation, providing the foundation for the multi-objective optimization of the auxiliary stator-type magnetizing device with multiple degrees of freedom.

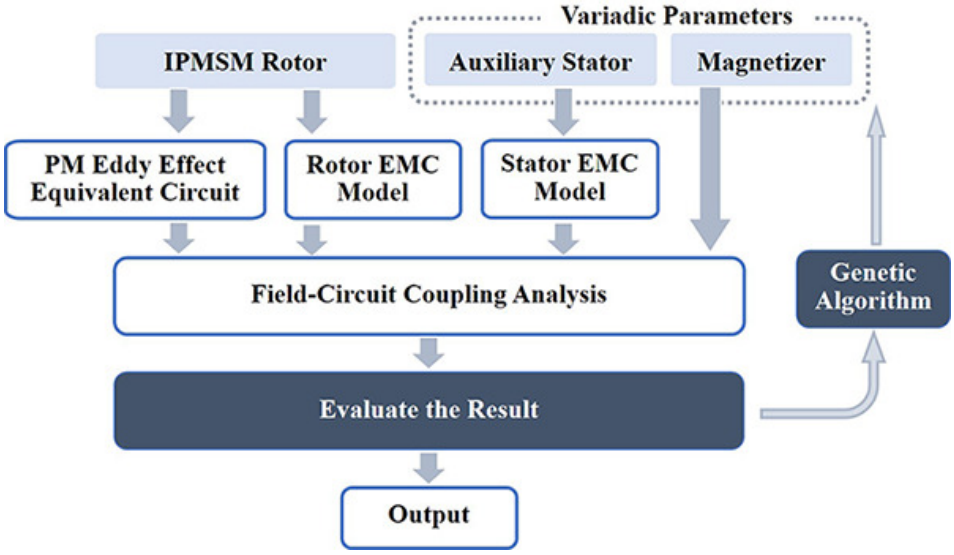

Figure 11. Stages and processes of the design method.

The six degrees of freedom mentioned in Section 2 are considered for optimizing the device. To fully magnetize the PMs, the peak flux density B_{PM_min} at the bottom region of the V-type PM is estimated with the rotor MEC model and is required to be above 3 T. Meanwhile, a pulse width of the order of millisecond is also essential. Provided that the

magnetizing ability is sufficient, the lower the volume, cost, and energy consumption, the better. Thus, the objective function f_{obj} and the constraints are:

$$\begin{aligned} min \;\; & f_{\text{obj}} = b_1 r_{\text{so}} + b_2 NS_{\text{wire}} + b_3 W_{\text{M}} \\ s.t. & \begin{cases} B_{\text{PM_min}} \geq 3\text{T} \\ T_{\text{M}} \geq 1\text{ms} \end{cases} \end{aligned} \tag{44}$$

where b_1, b_2, and b_3 are the weights corresponding to the indicators, r_{so} is the indicator of device volume, NS_{wire} is the indicator of copper quantity of the fixture which is a significant part of the device cost, and W_{M} is the energy consumption, which can be calculated by (3).

A genetic algorithm (GA) is used for the global searching of the optimal solution. A population of 40 potential solutions, also called individuals, is randomly generated as the first generation. The performance of each individual is calculated with the FCCA method, and a penalty term f_{pen} is introduced to transform the optimization problem into an unconstrained one:

$$f_{\text{pen}} = b_4 \left[\frac{3\,\text{T}}{\min(B_{\text{PM_min}}, 3\,\text{T})} - 1 \right] + b_5 \left[\frac{1\,\text{ms}}{\min(T_{\text{M}}, 1\,\text{ms})} - 1 \right] \tag{45}$$

where b_4 and b_5 are the weights corresponding to the indicators. Therefore, the fitness function S is obtained:

$$S = S_0 - f_{\text{obj}}(r_{\text{so}}, N, S_{\text{wire}}, W_{\text{M}}) - f_{\text{pen}}(B_{\text{PM_min}}, T_{\text{M}}) \tag{46}$$

where S_0 is the fitness baseline, which is used to adjust the exploration and convergence speed of the GA. The tournament selection is adopted to form a new generation, where the best individual always makes it into the next generation and the remaining individuals undergo the roulette-wheel selection. Crossover and mutation steps are then performed with the probability of 0.4 and 0.01, respectively.

The convergence of the optimization process is shown in Figure 12, where the fitness gradually increases and stabilizes at a value with the 44th generation. The individuals of the last 10 generations, the Pareto frontier, and the selected solution are shown in Figure 13 with the three objectives involved. Then, an individual of the Pareto frontier with high fitness value, suitable wire gauge, and appropriate magnetizer capacitance is selected as the final solution. The parameters of the obtained auxiliary stator-type magnetizing device are shown in Table 2.

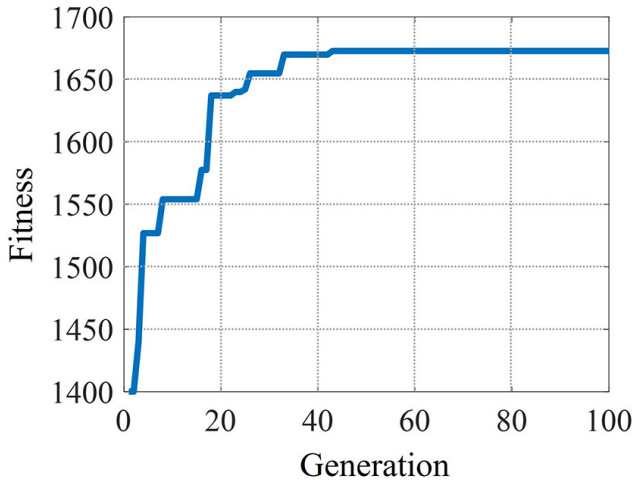

Figure 12. Convergence of fitness with generation.

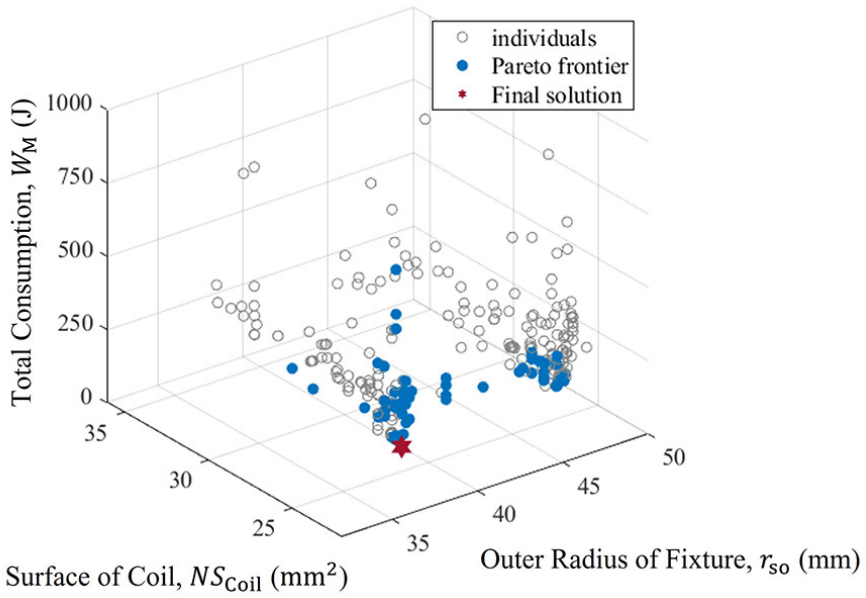

Figure 13. Individuals of last 10 generations, Pareto frontier, and selected solution.

The optimized design is compared to an empirical design that is being used in a factory. The empirical design has the same outer diameter r_{so} and the number of turns N as the optimized design, but differs in the shape of the auxiliary stator and the arrangement of the coils. The winding resistance and inductance of the two device designs are similar. The magnetizer capacitance adopted by the empirical design is also consistent with the optimized design.

Table 2. Parameters of the optimized auxiliary stator-type magnetizing device

Parameter Name	Parameter Value
Number of poles	4
Air gap length	0.5 mm
Auxiliary stator outer diameter	72.4 mm
Auxiliary stator inner diameter	43 mm
Auxiliary stator length	46.2 mm
Pole angle	43 degree
Pole length	4.4 mm
Yoke thickness	6.6 mm
Number of coil layers	2
Number of turns per coil	10
Number of parallel branches	1
Wire gauge	1.8 mm
Bare wire diameter	1.5 mm
Magnetizer capacitance	2 mF
Discharging voltage	700 V
Auxiliary stator material	Silicon Laminations

Ansys Maxwell is used to simulate the magnetization of both designs, and the discharging voltage is set to 700 V. In Figure 14a, the flux density of the PMs is above 3 T in most areas, which indicates the PMs are close to saturation. Compared with Figure 14b, the optimized design has been better magnetized. The reason is that the pole width of the empirically designed stator is equal to the angle of the top of V-type PM, which means that slots must be deeper to accommodate the coils. Consequently, the yoke is relatively thin and becomes more saturated during the magnetization. Figure 15 compares the flux density distribution at the PMs' middle line, which is drawn with black dotted lines in

Figure 14. The narrower pole adopted in the optimized stator helps to concentrate the magnetic field into the middle, which has a better magnetizing effect in the bottom region.

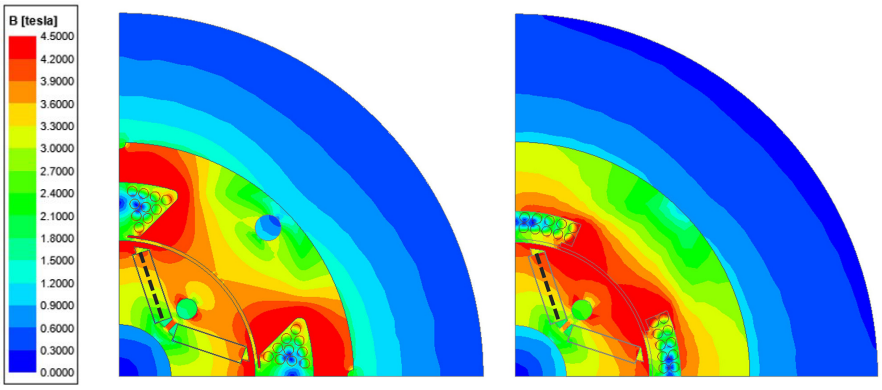

Figure 14. Comparison of the two device designs when the capacitance is 2 mF and discharge voltage is 700 V. (**a**) Flux density map of empirical design. (**b**) Flux density map of optimized design.

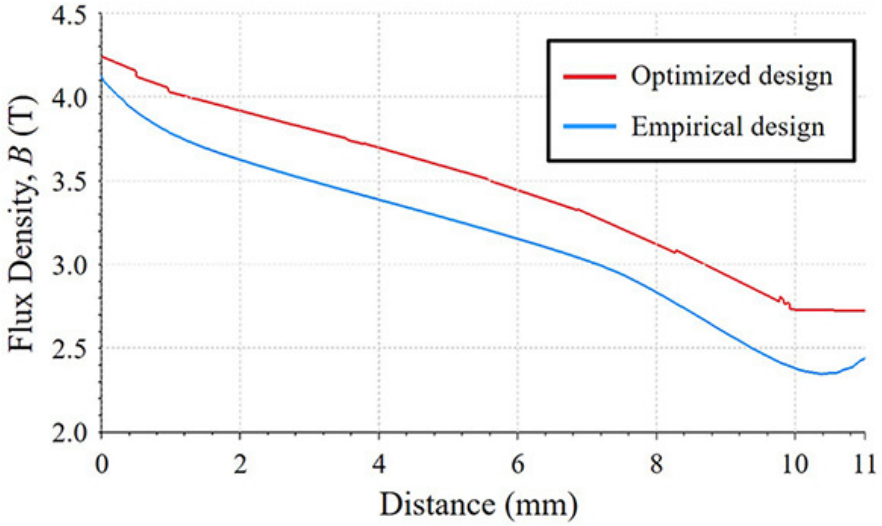

Figure 15. Peak value distribution of flux density in PMs along width direction.

5. Experiment

An empirically designed device and a prototype of the optimized design are tested with the 2 mF source shown in Figure 16, which is composed of eight 250 µF capacitors. The magnetizing winding of the fixture is stabilized with epoxy resin curing to prevent the deformation of the coil end turns.

An increasing initial voltage is set to the magnetizer to find the minimal energy for full magnetization. Since the repeated unsaturated magnetization of the same PM will increase the remanence, new unmagnetized PMs produced in the same batch are used for each magnetization in the experiments. After each completion of magnetization, all eight PMs are taken out from the rotor, placed in the center of a Helmholtz coil, and quickly pulled out. A voltage is induced in the Helmholtz coil as the flux linkage changes. Thus, the magnetic flux is obtained by integrating the induced voltage $E_{\mathrm{H}}(t)$, and the magnetic moment M of a PM is calculated as follows [19]:

$$\mu_0 M = \alpha \cdot \int E_{\mathrm{H}}(t)\mathrm{d}t \tag{47}$$

with α the coil constant of the Helmholtz coil.

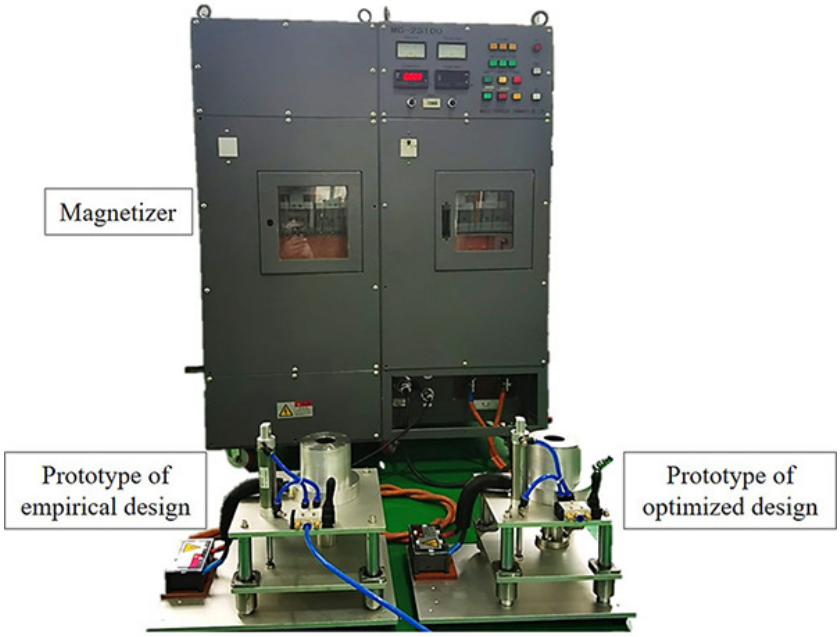

Figure 16. Magnetizer and prototypes.

As illustrated in Figure 17, the magnetic moment M of the PMs magnetized by the optimized design reaches its saturation at 600 V, which is slightly less than the 700 V estimated by the proposed circuit–field coupling analysis. To evaluate the magnetization completeness with the two post-assembly magnetizing devices, PMs that are fully magnetized in the factory are used as a reference; these are also further referred to as pre-magnetized PMs. The black dotted line indicates the magnetic moment M on the pre-magnetized PMs, and the coincidence indicates that the post-assembly magnetization achieves the same effect of the pre-magnetization. The results of the empirical design are also tested where the PMs are unsaturated until 1000 V. Comparatively, the voltage required by the optimized design is 60% of that by the empirical design. According to (3), the energy consumption W_M of the optimal design is 360 J, while that of the empirical design is 1000 J, which means that 64% of the energy is saved. Additionally, the aging of the insulation paper and the wires is slowed down thanks to the decrease in electro-thermal stress, thereby preventing insulation breakdown and increasing the device's lifespan [20–22].

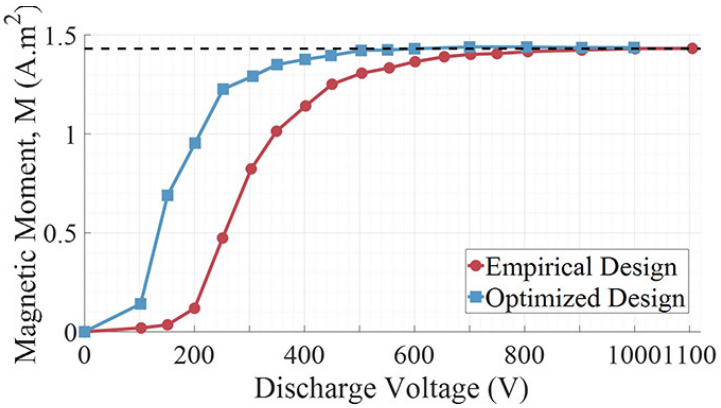

Figure 17. Flux generated by post-magnetized PMs with discharge voltage for empirical design and optimized design.

Considering the uneven distribution of the magnetizing field throughout the PMs, the surface flux density of the PMs is sampled with a Gauss meter. Four positions on the

front and back sides of the top and bottom regions of the V-shaped PM are selected as sampling points, as shown in Figure 18a. PMs magnetized with both devices are tested and the surface flux density is compared in Figure 18b. The surface flux density at points B and D is lower than that at points A and C, indicating that the bottom region of the PMs is more difficult to magnetize when the discharge voltage is insufficient; several values measured at the bottom region are negative due to the field generated by the top region being closed through to the bottom region. Therefore, special attention should be paid to the bottom region for the magnetization of V-type IPMSMs. Comparing the result of the two designs, the empirical design has a similar saturation voltage to the optimized design at points A and C, while the difference in saturation voltage at points B and D is much larger. Consequently, as validated in the optimal design, the narrow pole is advised for the magnetizing devices of V-type IPMSM, whilst the multi-parameter optimization design should be performed.

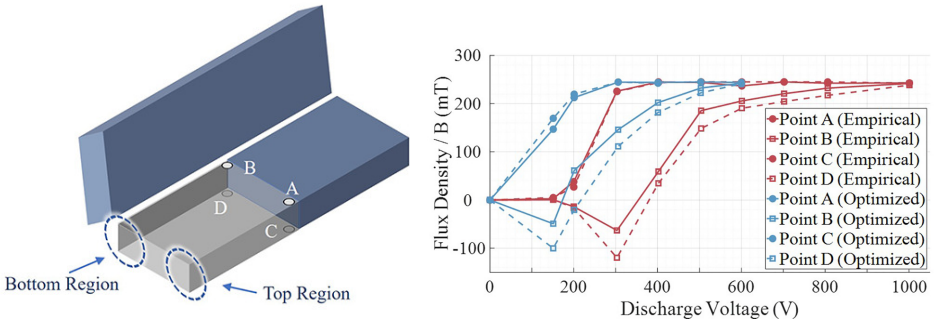

Figure 18. Flux density of post-assembly PMs at different sampling points. (**a**) Positions of sampling points of a PM. (**b**) Comparison of the flux density at different sampling points under empirical design and optimal design.

Moreover, the flux density on the surface of the magnetized V-type PM rotor is measured. A rotor with the pre-magnetized PMs is used as the reference, and the rotors with unmagnetized PMs are magnetized with both prototypes at 2 mF and 600 V for comparison. The surface magnetic flux density of the three rotors is shown in Figure 19. The rotor surface flux density of the optimized prototype almost coincides with that of the pre-magnetized PMs, indicating that the PMs achieve saturation with the proposed design. In contrast, the flux density of the empirical design is slightly lower. The results of the rotor surface flux density are consistent with the experiments above.

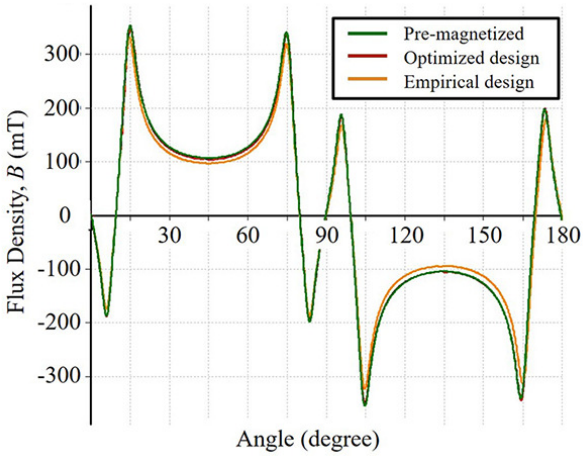

Figure 19. Measured flux density distribution at the rotor surface with pre-magnetized PMs, and with the PMs post-magnetized with the optimized and empirically designed devices.

6. Conclusions

A design method of an auxiliary stator-type magnetizing device based on the FCCA is proposed. The highly saturated iron core and the eddy currents inside the PMs are considered with equivalent models. It is verified that the results of the FCCA have an excellent agreement with the FEA and experimental results. The fast computing ability of the FCCA model allows for rapid global searching optimization of the magnetizing device. A multi-objective optimized solution is successfully obtained with a GA, resulting in a 40% reduction of the capacitor voltage and a 64% reduction of the energy consumption when compared with the empirical design. Therefore, this design method may become a valuable tool to accelerate the discovery of optimal solutions, which is not limited to V-type IPMSMs, and which can help the designer to clarify the intricate interactions between the parameters of the rotor and the magnetizing device.

In this paper, the optimization method of a V-type IPMSM is proposed, with a focus on the magnetic field. In further research, the coil stress and temperature rise caused by the large currents will be studied. To this end, a multi-physics model combining magnetic, heat transfer, and mechanical aspects will be established, and more objectives and constraints will be considered in the optimization process.

Author Contributions: Conceptualization, J.-X.S. and Z.-A.Z.; methodology, Z.-A.Z. and X.-F.Q.; software, Z.-A.Z. and L.Y.; validation, Z.-A.Z. and Y.-C.W.; formal analysis, Z.-A.Z.; investigation, Z.-A.Z.; resources, J.-X.S. and Y.-C.W.; data curation, Z.-A.Z.; writing—original draft preparation, Z.-A.Z.; writing—review and editing, J.G. and Z.-A.Z.; visualization, Z.-A.Z.; supervision, J.-X.S.; project administration, J.-X.S.; funding acquisition, J.-X.S. All authors have read and agreed to the published version of the manuscript.

Funding: This work was supported by the National Key Research and Development Program of China grant number 2022YFB3403100.

Institutional Review Board Statement: Not applicable.

Data Availability Statement: The data presented in this study are available on request from the corresponding author. The data are not publicly available due to privacy.

Conflicts of Interest: The authors declare no conflicts of interest.

Abbreviations

The following abbreviations are used in this manuscript:

PM	Permanent Magnet
FEA	Finite Element Analysis
FCCA	Field–Circuit Coupling Analysis
IPMSM	Interior Permanent Magnet Synchronous Motor
MEC	Magnetic Equivalent Circuit
SPMSM	Surface-Mounted Permanent Magnet Synchronous Motor
MMF	Magnetomotive Force
FE	Finite Element
GA	Genetic algorithm

References

1. Dorrell, D.G.; Hsieh, M.F.; Hsu, Y.C. Post Assembly Magnetization Patterns in Rare-Earth Permanent-Magnet Motors. *IEEE Trans. Magn.* **2007**, *43*, 2489–2491. [CrossRef]
2. Li, L.; Huang, X.; Wu, A.; Thompson, P.; Ranze, R.; Yu, H.; Laskaris, T.; Amm, K. Development of a Large Bore Long Pulse Magnet at GE Global Research Center. *IEEE Trans. Appl. Supercond.* **2006**, *16*, 1672–1675. [CrossRef]
3. Kim, K.S.; Park, M.R.; Kim, H.J.; Chai, S.H.; Hong, J.P. Estimation of Rotor Type Using Ferrite Magnet Considering the Magnetization Process. *IEEE Trans. Magn.* **2016**, *52*, 8101804. [CrossRef]
4. Hsieh, M.F.; Hsu, Y.C.; Chen, P.T. Analysis and Experimental Study of Permanent Magnet Machines with In-Situ Magnetization. *IEEE Trans. Magn.* **2013**, *49*, 2351–2354. [CrossRef]

5. Hsieh, M.F.; Hsu, Y.C.; Dorrell, D.G. Design of Large-Power Surface-Mounted Permanent-Magnet Motors Using Postassembly Magnetization. *IEEE Trans. Ind. Electron.* **2010**, *57*, 3376–3384. [CrossRef]
6. Wang, Q.; Ding, H.; Zhang, H.; Zhou, J.; Wang, G.; Lv, Y.; Li, L. Research of Post-Assembly Magnetization of Large-Power Surface-Mounted Rare-Earth Permanent Magnet Machines With Integrated Magnetizing Winding. *IEEE Trans. Appl. Supercond.* **2020**, *30*, 5204505. [CrossRef]
7. Ho, S.L.; Li, H.L.; Fu, W.N. A Post-Assembly Magnetization Method of Direct-Start Interior Permanent Magnet Synchronous Motors and Its Finite-Element Analysis of Transient Magnetic Field. *IEEE Trans. Magn.* **2012**, *48*, 3238–3241. [CrossRef]
8. Fu, W.N.; Chen, Y. A Post-Assembly Magnetization Method for a Line-Start Permanent-Magnet Motor. *IEEE Trans. Appl. Supercond.* **2016**, *26*, 0602604. [CrossRef]
9. Lv, Y.; Xia, D.; Wang, Q.; Li, L. Post-assembly magnetization of high speed PM rotor with metallic sleeve. In Proceedings of the 2017 20th International Conference on Electrical Machines and Systems (ICEMS), Sydney, Australia, 11–14 August 2017; pp. 1–5. [CrossRef]
10. Angara, R.C.S.B.; Hsu, K.W.; Villar, P.J.; Sheth, N.K. Influence of Soft Magnetic Material Type in Fixture Components on the Magnetization of Bonded Neo Magnet and Motor Performance. *IEEE Trans. Magn.* **2018**, *54*, 2101305. [CrossRef]
11. Lv, Y.; Yang, Y.; Xia, D.; Xu, B.; Peng, T.; Xiao, H.; Li, L. Saddle-Shaped Post-Assembly Magnetization Coil for a 300 kW 2-Pole High-Speed Permanent Magnet Rotor. *IEEE Trans. Appl. Supercond.* **2020**, *30*, 5206705. [CrossRef]
12. Kwon, S.J.; Lee, B.H.; Kim, K.S.; Jung, J.W. Design Process of Post-Assembly 3-Times Magnetizer for 10-Poles of Flux Concentrated Rotor Considering Eddy Current Effect. *IEEE Access* **2023**, *11*, 34476–34485. [CrossRef]
13. Lee, C.; Kwon, B.; Kim, B.T.; Woo, K.; Han, M. Analysis of magnetization of magnet in the rotor of line start permanent magnet motor. *IEEE Trans. Magn.* **2003**, *39*, 1499–1502. [CrossRef]
14. Lee, C.K.; Kwon, B.I. Design of post-assembly magnetization system of line start permanent-magnet motors using FEM. *IEEE Trans. Magn.* **2005**, *41*, 1928–1931. [CrossRef]
15. Wang, Q.; Ding, H.; Zhang, H.; Lv, Y.; Guo, H.; Li, L. Study of a Post-Assembly Magnetization Method of a V-Type Rotor of Interior Permanent Magnet Synchronous Motor for Electric Vehicle. *IEEE Trans. Appl. Supercond.* **2020**, *30*, 5206205. [CrossRef]
16. Negahdari, A.; Toliyat, H.A. Post-assembly magnetization of rare-earth permanent magnet materials in permanent magnet assisted synchronous reluctance motors. In Proceedings of the 2017 IEEE International Electric Machines and Drives Conference (IEMDC), Miami, FL, USA, 21–24 May 2017; pp. 1–6. [CrossRef]
17. Hsieh, M.F.; Lien, Y.M.; Dorrell, D.G. Post-Assembly Magnetization of Rare-Earth Fractional-Slot Surface Permanent-Magnet Machines Using a Two-Shot Method. *IEEE Trans. Ind. Appl.* **2011**, *47*, 2478–2486. [CrossRef]
18. Bland, D.R. The Method of Separation of Variables. In *Solutions of Laplace's Equation*; Bland, D.R., Ed.; Springer: Dordrecht, The Netherlands, 1961; pp. 15–28. [CrossRef]
19. Trout, S. Use of Helmholtz coils for magnetic measurements. *IEEE Trans. Magn.* **1988**, *24*, 2108–2111. [CrossRef]
20. Ramu, T.S. On the Estimation of Life of Power Apparatus Insulation Under Combined Electrical and Thermal Stress. *IEEE Trans. Electr. Insul.* **1985**, *EI-20*, 70–78. [CrossRef]
21. Sun, P.; Sima, W.; Yang, M.; Wu, J. Influence of thermal aging on the breakdown characteristics of transformer oil impregnated paper. *IEEE Trans. Dielectr. Electr. Insul.* **2016**, *23*, 3373–3381. [CrossRef]
22. Polyakov, D.A.; Nikitin, K.I.; Novozhilov, A.N.; Kletsel, M.Y. Research of Electro-Thermal Aging Process of Cross-Linked Polyethylene. *J. Phys. Conf. Ser.* **2018**, *1050*, 012061. [CrossRef]

Disclaimer/Publisher's Note: The statements, opinions and data contained in all publications are solely those of the individual author(s) and contributor(s) and not of MDPI and/or the editor(s). MDPI and/or the editor(s) disclaim responsibility for any injury to people or property resulting from any ideas, methods, instructions or products referred to in the content.